Hindawi
Wireless Communications and Mobile Computing
Volume 2017, Article ID 1830987, 14 pages
https://doi.org/10.1155/2017/1830987

*Research Article*

# Feasibility Studies on the Use of Higher Frequency Bands and Beamforming Selection Scheme for High Speed Train Communication

**Ayotunde O. Laiyemo, Petri Luoto, Pekka Pirinen, and Matti Latva-aho**

*Centre for Wireless Communications, University of Oulu, P.O. Box 4500, 90014 Oulu, Finland*

Correspondence should be addressed to Ayotunde O. Laiyemo; ayotunde.laiyemo@oulu.fi

Received 26 May 2017; Accepted 20 July 2017; Published 28 August 2017

Academic Editor: Cesar Briso



With increasing popularity of high speed trains and traffic forecast for future cellular networks, the need to provide improved data rates using higher frequency bands (HFBs) for train passengers is becoming crucial. In this paper, we modify the OFDM frame structure for HST, taking into account the increasing sensitivity to speed at HFBs. A lower bound on the SNR/SINR for a given rate for reliable communication was derived considering the physical layer parameters from the OFDM frame. We also analyze different pathloss models in the context of examining the required gain needed to achieve the same performance as with microwave bands. Finally, we present a time-based analogue beamforming selection approach for HST. We observed that, irrespective of the pathloss models used, the required gains are within the same range. For the same SNR/SINR at different frequency bands, the achievable data rate varies with respect to the frequency bands. Our results show the potential of the use of HFBs. However, due to the increased sensitivity of some channel parameters, a maximum frequency band of 38 GHz is suggested. Evaluation of our proposed beamforming scheme indicates a close performance to the optimal SVD scheme with a marginal rate gap of less than 2 b/s/Hz.

## 1. Introduction

The increasing interest in the deployment of high speed trains (HSTs) in many parts of the world has evoked the need to provide high quality wireless communication services to onboard users. Following the recent trends and forecast in broadband communications, traffic from wireless and mobile devices will account for two-thirds of the total traffic and the required data rates will nearly double by 2020 [1]. It is obvious by direct extension that the HST passengers travelling in large groups for extended period of time will also need access to bandwidth hungry applications particularly multimedia services. However, providing such high data rates and good quality of service (QoS) to passengers in the presence of rapidly varying channel conditions and scarce bandwidth availability in the current cellular network is a challenging task [2, 3].

Enabling advanced multiantenna and multiplexing schemes with efficient use of available spectrum has been a subject of extensive research. Hence, some of these techniques such as advanced multiple-input multiple-output (MIMO), coordinated multipoint (CoMP), and carrier aggregation (CA) have been adopted in most wireless standards, such as IEEE 802.16e/m and 3GPP LTE/LTE-A [4]. Due to the scarce available bandwidth at microwave frequency bands, the use of these techniques is not enough to achieve the rapid growing required data rates. Therefore, the wireless communications community steers its focus towards higher frequency bands (HFBs) (between 6 and 100 GHz) for the 5th-generation (5G) wireless communications, since the large available bandwidth at HFBs has been seen as a potential to meet the incredible data rate demand [5]. The use of HFBs has previously been limited to indoor applications [6] due to its sensitivity to the atmosphere and severe propagation loss, which is inversely proportional to the squared wavelength, thereby affecting long range transmission [7]. With the small wavelength and recent advances in modular antenna array technology for HFBs, high beamforming gains can

be obtained to combat large propagation loss and therefore are potentially suitable for outdoor communication as demonstrated in [8], where a distance of up to 1 km is achieved for mm-wave link transmission. Advances in modular antenna array technology allow the creation of large antenna array with high gain in a cost effective and scalable manner [9]. Furthermore, the measurements campaign in [5, 10–12], showed that the mm-wave band can be a good candidate for the next generation 5G cellular systems, with a focus on urban environment.

Motivated by these channel measurements and expectations, several studies have put in effort to develop algorithms to estimate the HFB channel parameters that exploit the peculiar nature of the channel [13–15] and design beamforming algorithms [16–18] to increase the achievable data rates. However, majority of these researches focus on urban small cell deployment scenario with cell sizes of 50 to 200 meters, which in the case of the HST scenario would result in handovers every few seconds. Also, the adaptive beamwidth beamforming algorithms and codebook designs in [16–18], which require beam training time, cannot be directly used for the HST scenario, because the HFB channels are more sensitive to channel state information feedback delay due to the fast time-varying channel caused by high mobility [19].

The use of HFBs for HST and 5G communication system for railway (5G-R) was suggested in [20] with the goal of providing larger bandwidth and higher data rate transmission capability. In [21], a hybrid spatial modulation beamforming scheme is proposed at HFBs under the HST scenario, where a combination of spatial modulation and hybrid beamforming is used to enhance rate performance. However, channel state information feedback delay was not taken into account, which can significantly affect the rate performance. A modification to the IEEE 802.11ad beam sweeping approach was examined in [22], where the number of beams and an optimum repetition time to sweep through the beams were determined from the velocity estimate of the HST. Also HFB beam switching support for HSTs was considered in [23], in which the beam switching approach leverage on the knowledge of the train position in optimizing the beamwidth to achieve a higher rate. However, information of the selected beam at the BS is required at the HST and beam design details were not examined.

In this paper, we first focus on analyzing the impact and feasibility of the use of different frequency band for HST scenario. We derive a lower bound SNR/SINR curve to achieve a successful transmission for a given target rate. We also propose an improved frame structure based on orthogonal frequency division multiplexing (OFDM) for the HST scenario, such that the maximum speed of the HST and the carrier frequency used are taken into account. Motivated by the rural macrocell (RMa) channel measurement carried out in [24] for HFBs and the remarkable coverage achieved using the close-in (CI) reference distance pathloss model, we analyze the impact of different pathloss models on a range of carrier frequencies, since the lower bound SNR/SINR curve is affected by the pathloss.

The pathloss model proposed for channel models for HFBs (6–100 GHz) in 3GPP released TR 38.900 [25] and the pathloss model proposed for mm-wave communications in [24, 26] have been considered as appropriate pathloss models for HFBs (>6 GHz). Hence, these two pathloss models are analyzed and compared along with two other pathloss models assumed not suitable for HFBs: free space pathloss model and modified IEEE 802.16 pathloss model. We also examine the effect of these pathloss models in an interference limited scenario.

Finally, we propose a simplified analogue beamforming selection approach based on the properties of the railway environment and the HFB channel. An ordered codebook is developed using an array response vector with a range of angles and a distance/time-based selection approach is used to select the optimal beamforming weight and receive filter at any given time instance. The contributions of this paper are summarized as follows:

(i) We modify the OFDM frame structure for HST, taking into consideration the properties of HFBs and the high velocity of the HST. The modification of the OFDM frame reveals the increased sensitivity to intersymbol interference (ISI) and intercarrier interference (ICI) at HFBs.

(ii) We generate a lower bound SNR/SINR curve for successful transmission using the modified OFDM framework at HFB for a given maximum train speed.

(iii) We establish a performance gap between different pathloss models for HFBs in terms of the required gain needed to achieve the same performance at microwave bands.

(iv) We design a sequentially ordered codebook at HFB for HST. The codebook relies on the array response vector with ordered angular inputs generated from a range of possible AoA/AoD.

(v) We propose a distance/time-based analogue beamforming selection scheme for HST. This scheme leverages on LOS propagation and the prior knowledge of the HST position and velocity.

(vi) We analyze the performance of the proposed beamforming scheme in comparison with the optimal SVD beamforming approach and the state-of-the-art LTE based closed-loop precoding method.

The rest of this paper is organized as follows. In Section 2, the background and suitability studies of the use of HFBs for HST networks are examined. The system model for the HST network is introduced in Section 3. The proposed beamforming selection scheme as applied to the HST is presented in Section 4. In Section 5, the simulation results are discussed and the conclusion is provided in Section 6.

## 2. Background and Feasibility Studies

*2.1. The Railway Deployment Scenario.* The railway deployment scenario targets continuous coverage and high data rates to mobile users inside a HST along the rail track. Mobile users include onboard passengers who require high data rates and essential train communication devices which require

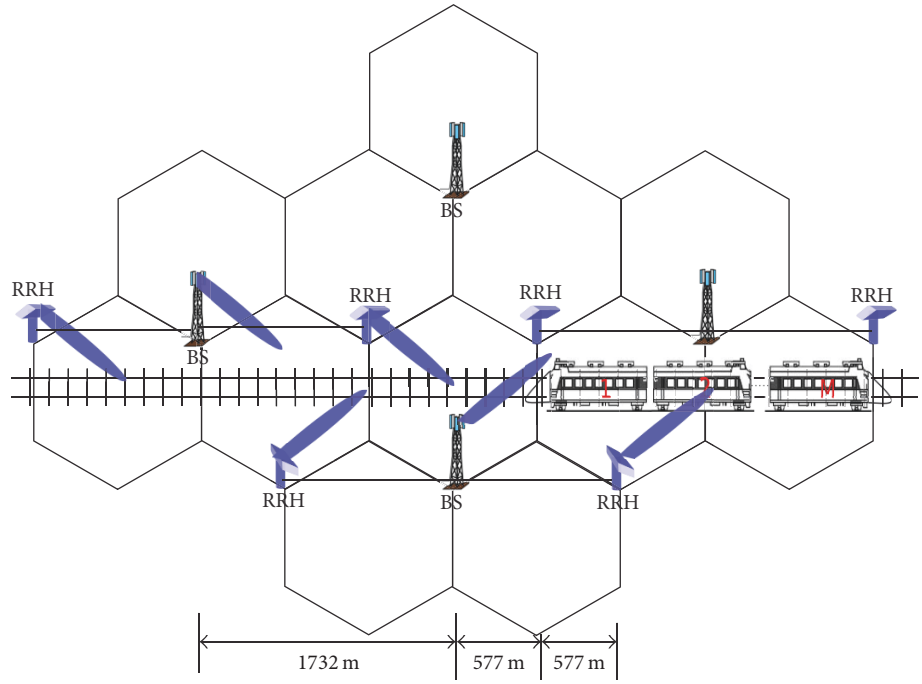


Figure 1: HST scenario with RRHs to ensure LOS propagation.

high reliability [27]. To guarantee reliable communication in a HST network, knowledge about the high speed railway environment is required. The propagation characteristics of the railway environment have been observed in a number of studies through channel measurements and analyses at microwave frequency bands [28–34]. For most of the railway propagating environment, strong LOS component is present and there are few multipaths because of little scatterers and reflections closely similar to the rural macrocell (RMa) propagation scenario described in [35]. Considering HFBs for HST scenario and maintaining the network layout for microwave bands so as not to increase the strain on the existing challenge of frequent handover, the LOS component will be lost for most paths and NLOS components will be negligible due to fewer scatters. However, remote radio heads (RRHs) and moving relay nodes (MRNs) on the HST can be used to ensure the presence of LOS propagation as proposed in [36] and shown in Figure 1.

Previous studies in [37] identified the critical differences between the railway communication system and the conventional cellular system with the proposed transmission schemes for the HST scenario using a two-hop network architecture. A single hop network architecture was adopted in [38], where advanced collaboration schemes were used to improve the throughput. However, with the increasing data rate requirement, the use of advanced transmission schemes and techniques at microwave bands is not enough to meet the data rate demand. Hence, the large available bandwidth at higher operating frequency bands is seen as a potential to meet the data rate demand in the railway deployment scenario.

Hence, the impact of high mobility and additional pathloss must be taken into account in the choice of HFB to ensure proper communication network planning. Also, the increased impact of the delay spread and Doppler shift/spread must be taken into account in the development of the OFDM frame structure when HFBs are considered.

*2.2. Higher Frequency Band Frame Structure for HST.* The design of a 5G new radio physical layer is heavily influenced by the requirements for high data rate, improved spectral efficiency, and the availability of larger channel bandwidths. To fulfil these requirements, OFDM frame structure is proposed as a good candidate. Also, some advanced technical features of LTE-A are being considered for 5G systems, such that 5G is designed to exploits ways to combine existing 4G LTE networks with capabilities provided by 5G [39]. Hence, the existing LTE framework is used as a guide in the development of the HFB frame structure for HST. The development of the frame structure for HST is vital in predicting accurate lower bound on SNR/SINR for a given target rate. We propose the use of the modified alpha Shannon formula [40] to facilitate accurate benchmarking of the OFDM structure such that the physical layer parameters are taken into account in deriving the minimum SNR/SINR value for successful transmission for a given target rate. The minimum SNR/SINR for successful transmission can be expressed as

$$\Gamma = \beta\left(2^{R_{\text{tar}}/\alpha B} - 1\right), \tag{1}$$

where $R_{\text{tar}}$ is the target rate and $B$ is the transmission bandwidth. The symbol $\beta$ represents the SNR efficiency

Table 1: Frame structure parameters for a maximum speed of 500 km/h.

| Frequency (GHz) | 2 | 10 | 28 | 30 | 38 | 73 |
|---|---|---|---|---|---|---|
| Frame duration (ms) | 10 | 10 | 10 | 10 | 10 | 10 |
| Subframe duration (ms) | 1 | 1 | 1 | 1 | 1 | 1 |
| Length of cyclic prefix $T_{\mathrm{CP}_1}$ ($\mu$s) | 5.2 | 5.2 | 5.2 | 5.2 | 5.2 | 5.2 |
| Length of cyclic prefix $T_{\mathrm{CP}_2}$ ($\mu$s) | 4.7 | 4.7 | 4.7 | 4.7 | 4.7 | 4.7 |
| Doppler frequency $F_D$ (kHz) | 0.93 | 4.63 | 13 | 14 | 17.6 | 33.8 |
| Sub-carrier spacing $\Delta f$ (kHz) | 15 | 18.8 | 60 | 60 | 71.3 | 138.8 |
| Length of symbol $T_u$ ($\mu$s) | 66.7 | 53.2 | 16.7 | 16.7 | 14 | 7.2 |
| Number of symbol $N_{\mathrm{sym}}$ | 7 | 9 | 23 | 23 | 28 | 42 |
| Resource block (RB) size (kHz) | 180 | 225.6 | 720 | 720 | 855.6 | 1665.6 |
| Resource elements per RB | 84 | 108 | 276 | 276 | 336 | 504 |
| Number of pilot symbols per RB | 4 | 6 | 12 | 12 | 14 | 22 |

factor, which is partly a function of the used modulation and coding scheme and performance aspect of the receiver algorithms. Hence, SNR efficiency factor can be extracted using curve fitting to link-level simulations [40]. The symbol $\alpha$ represents the system bandwidth efficiency factor. The bandwidth efficiency factor quantifies the available bandwidth that can be used for transmission. It takes into account the overhead of the following physical layer parameters [41]: the cyclic prefix, the pilot assisted channel estimation, common control channels, and adjacent channel leakage ratio (ACLR) requirements. Based on these parameters, the bandwidth efficiency factor is expressed as

$$\alpha = \left(1 - N_{\mathrm{cp}}\right)\left(1 - N_{\mathrm{pilot}}\right)\left(1 - N_{L1/L2}\right)\left(1 - N_{\mathrm{ACLR}}\right), \quad (2)$$

where $N_{\mathrm{cp}}$, $N_{\mathrm{pilot}}$, $N_{L1/L2}$, and $N_{\mathrm{ACLR}}$ represent percentage overhead of the corresponding physical layer parameters.

Due to the high speed of the train and the shorter wavelength of higher operating frequency bands, the OFDM frame structure needs to be defined for HFBs such that the subcarrier spacing $\Delta f$ is adjusted with the following constraints:

$$\Delta f \ll \frac{1}{T_{\mathrm{CP}}}, \qquad \Delta f \gg f_D, \quad (3)$$

where $T_{\mathrm{CP}}$ and $f_D$ represent the length of cyclic prefix and the maximum Doppler shift, respectively.

We propose that the 5G new radio frame should maintain the LTE radio frame of 10 ms with a subframe of 1 ms and a time slot of 0.5 ms, and the subcarrier spacing for the HFBs is also constrained such that the sampling rate is a multiple or submultiple of the WCDMA chip rate of 3.84 Mcps. Furthermore, the number of OFDM symbols in one time slot will be affected by change in subcarrier spacing since the length of the useful symbol $T_u = 1/\Delta f$. The number of OFDM symbols is given as

$$N_{\mathrm{sym}} = \frac{T_{\mathrm{slot}} - \left(T_u + T_{\mathrm{CP}_1}\right)}{T_u + T_{\mathrm{CP}_2}} + 1, \quad (4)$$

where $T_{\mathrm{slot}}$ is the time slot, $T_{\mathrm{CP}_1}$ is the length of cyclic prefix for the first symbol in each time slot, and $T_{\mathrm{CP}_2}$ is the length of cyclic prefix for the rest of the symbols. Hence, $N_{\mathrm{cp}}$ is affected by the ratio of $T_{\mathrm{CP}}$ and $T_u$.

Still using the LTE framework as a guide, transmission is scheduled by resource blocks (RB) each of which consists of 12 consecutive subcarriers for a duration of one time slot. The pilot symbols for channel estimation are inserted in the OFDM time-frequency grid with a time domain spacing of four symbols and a frequency domain spacing of six subcarriers. Therefore, $N_{\mathrm{pilot}}$ is impacted by the number of pilot symbols and the number of resource elements in a time slot. We assume that the values of $N_{L1/L2}$ and $N_{\mathrm{ACLR}}$ are fixed irrespective of the carrier frequency used, since they are independent of the carrier frequency. Table 1 shows the derived 5G new radio physical layer parameters for different operating frequency bands using the LTE framework [42] as a guide and assuming a maximum mobile speed of 500 km/h.

From Table 1, we assume the same cyclic prefix length across all frequency bands despite the changes in the symbol length $T_u$. Without the cyclic prefix, an overlap of symbols, that is, ISI and loss of orthogonality between subcarriers, that is, ICI, can occur due to delay spread from multipath and Doppler spread from high velocity. However, HFBs are highly sensitive to high velocity leading to a significant shift of the received frequency. Therefore, the cyclic prefix, which is a duplication of a fraction of the symbol end, will use a larger fraction of the symbol for HFBs to compensate for the large shift. The considerable amount bandwidth consumed by the cyclic prefix can be tolerable due to the large available bandwidth at HFBs.

Furthermore, it is important to examine the fundamental relationship and impact of bandwidth and noise power on the achievable SNR/SINR to show the limits of increasing the channel bandwidth and provide an appropriate lower bound on SNR/SINR to achieve a successful transmission of a signal. If we assume a SISO link, the achievable data rate over the link is limited by the capacity of the link, which is a function of the bandwidth $B$ and the SNR $\Gamma$:

$$C = B \times \log_2\left(1 + \Gamma\right). \quad (5)$$

On the other hand, the SNR is a function of the received power $P_r$ and the noise power $N$. The noise power is proportional to the bandwidth given as

$$N = k \times T \times NF \times B. \quad (6)$$

From (5), increasing the bandwidth is a straightforward way to improve the achievable data rate. But the noise power also increases with an increase in bandwidth. Hence, with a fixed transmit power, a significant increase in bandwidth will lead to a significantly low SNR. A large increase in the transmit power could be seen as a solution. But large transmit power is inappropriate due to high power consumption, power amplifier requirements, heat-dissipation problems, and emission regulations [9]. Similarly, when multiple cells are considered, there is the presence of intercell interference $I$ and the achievable data rate is expressed as

$$R_{\text{acv}} = B \times \log_2\left(1 + \frac{P_r}{N + I}\right) = B \times \log_2(1 + \Gamma), \quad (7)$$

where the SNR is replaced with signal-to-noise plus interference ratio (SINR).

For a given fixed bandwidth, improved data rate can be achieved by ensuring high SINR. The achieved SINR on a given BS-UE link is dependent on the carrier frequency $f_c$ and the distance $d$ between the serving BS and UE, expressed as

$$\Gamma^b = \frac{P_r}{N + I} = \frac{P_t^b \times G_t^b \times 10^{-PL(f_c,d)/10}}{N + \sum_I \left(P_t^{b'} \times G_t^{b'} \times \delta^{b'} \times 10^{-PL(f_c,d_I)/10}\right)}, \quad (8)$$

where $P_t^b$ and $P_t^{b'}$ are the transmit powers from the serving BS and interfering BSs, respectively, $G_t^b$ and $G_t^{b'}$ are the transmit antenna gains at the serving BS and interfering BSs, respectively, $\delta^{b'}$ corresponds to the load factor estimated at the interfering BSs, and $PL(\cdot)$ is obtained from one of the pathloss models described in Section 2.3. The effect of carrier frequency on the minimum SNR/SINR for reliable transmission is shown in Section 5.

*2.3. Pathloss Models.* An appropriate pathloss model that predicts the propagation path in combination with a given target rate is required to estimate the minimum required SNR/SINR at a given distance for reliable transmission. Different pathloss models have been proposed for different propagation environment at microwave frequency bands and few have been extended and proposed for cm-wave and mm-wave frequency band. However, based on the characteristics of the railway propagation scenario, we focus our analysis on LOS pathloss models and examine the effect of increasing the operating frequency band. Four pathloss models are considered in this paper.

*(1) Free Space.* The free space pathloss model [43] reflects its dependency on distance and frequency. The dependency on distance is caused by the spreading out of signal energy in free space in which the signal strength is inversely proportional to the square of the distance travelled. The dependency on frequency anchors on the receiving antenna's effective area when we assume a fixed antenna gain. The antenna's effective area is proportional to the square of the wavelength. Hence, an increase in frequency will lead to a decrease in antenna's effective area and in turn lead to an increase in pathloss.

*(2) Modified IEEE 802.16.* The modified IEEE 802.16 pathloss model [44, 45] was developed by IEEE task group, based on extensive field measurements at 1.9 GHz in 95 existing macrocells across the USA. The model was mainly derived for three types of propagation scenario, namely, type A, type B, and type C. From the three types of propagation described, the type C scenario is used since it closely follows the railway scenario.

*(3) 3GPP RMa LOS.* The 3GPP RMa LOS pathloss model [25] was developed for the rural macropropagation scenario based on measurement results carried out in [35, 46–48]. The 3GPP RMa LOS is one of the pathloss models used in the calibration of channel models for HFBs with the aim of making the channel model cover a range of coupling loss considering typical cell sizes and the applicability of using HFBs to existing deployments.

*(4) CI Model.* The CI pathloss model [26, 49] is described as a generic all-frequency pathloss model that can easily be implemented in existing 3GPP models by replacing a floating non-physically based constant with a frequency dependent constant that represents free space pathloss at a given reference distance ($d_0$) of propagation. The reference distance $d_0$ can vary for different propagation environment. The CI pathloss model was originally adopted for urban microcell (UMi), urban macrocell (UMa), and indoor hotspot (InH) propagation scenarios described in [25]. However, the CI pathloss model has been extended and well suited for the RMa propagation scenario [24].

The first two models are generic pathloss models, which are assumed not to be suited for HFBs. However, we examine them to show some peculiar characteristics with the 3GPP RMa LOS model, which has been adopted for channel models with operating frequency bands between 6 and 100 GHz and with the CI model, which is strongly considered for mm-wave bands.

## 3. System Model for Beamforming Selection Scheme

We consider a train communication scenario with a focus on the BS-to-train link as shown in Figure 2. The train has multiple carriages, each equipped with a single moving relay node (MRN). The number of MRNs is denoted by $M$. The BS is equipped with $N_t$ transmit antennas with $N_{\text{rf}}$ RF chains such that $N_t$ is a multiple of $N_{\text{rf}}$. Each MRN is equipped with an external antenna array having $N_r$ receive antennas.

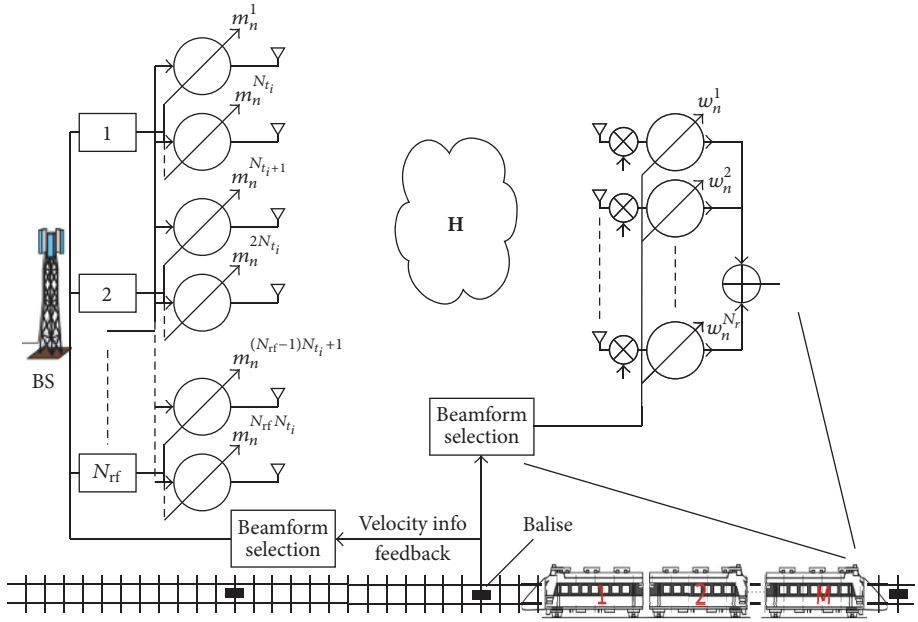


FIGURE 2: Single-cell train scenario.

Since HFB signals are mainly characterized by reflections and high sensitivity to absorption resulting in limited scatterers [12, 13], we adopt a statistical spatial channel model (SSCM) based on [50], where the generated channels have the feature of directionality [18]. Under this model, the channel matrix for the $c$th subcarrier can be expressed in terms of the transmit and receive array response vectors as

$$\mathbf{H}_c = \sqrt{\frac{N_t N_r}{L}} \sum_{l=1}^{L} \alpha_l \cdot \mathbf{\Phi}_l \otimes \mathbf{a}_r\left(\theta_l^{\mathrm{AoA}}\right) \mathbf{a}_t\left(\theta_l^{\mathrm{AoD}}\right)^H \cdot e^{-j2\pi c\tau_l}, \tag{9}$$

where $\alpha_l$ is the amplitude of the channel gain of the $l$th multipath component, $\mathbf{\Phi}_l \in \mathbb{C}^{N_r \times N_t}$, and $\tau_l$ denotes the phase matrix and time delay for the $l$th multipath component, respectively. $\mathbf{a}_r(\cdot)$ and $\mathbf{a}_t(\cdot)$ are the receive and transmit array response vectors, respectively, while $\theta_l^{\mathrm{AoD}}$ and $\theta_l^{\mathrm{AoA}}$ represent the angle of departure and the angle of arrival of the $l$th multipath component, respectively. The operator $\otimes$ represents the Hadamard product. The array response vector can be expressed as

$$\mathbf{a}\left(\theta_l\right) = \frac{1}{\sqrt{N}} \left[1, e^{jk\Delta \sin(\theta_l)}, \ldots, e^{j(N-1)k\Delta \sin(\theta_l)}\right]^T, \tag{10}$$

where $k = 2\pi/\lambda$, $\lambda$ is the carrier wavelength, and $\Delta$ is the antenna spacing. The RF chains are implemented such that the channel can be expressed as $\mathbf{H}_c = [\mathbf{H}_{c,1}, \ldots, \mathbf{H}_{c,N_{\mathrm{rf}}}]$, with $\mathbf{H}_{c,i} \in \mathbb{C}^{N_r \times N_{t_i}}$, where $N_{t_i} = N_t/N_{\mathrm{rf}}$. We assume that the number of data streams is equal to the number of RF chains.

The downlink received signal vector $\mathbf{y}_{c,i} \in \mathbb{C}^{N_r}$ at the $c$th subcarrier for the $i$th RF chain is given as

$$\mathbf{y}_{c,i} = \mathbf{H}_{c,i}\mathbf{m}_n s_{n,i} + \mathbf{n}, \tag{11}$$

where $\mathbf{H}_{c,i} \in \mathbb{C}^{N_r \times N_{t_i}}$ is the channel matrix of the $i$th RF chain between the serving BS and the MRN. The beamforming weight is given as $\mathbf{m}_n \in \mathbb{C}^{N_{t_i}}$, where the subscript $n$ is the index from a beamforming set $\mathscr{M}$ and $s_{n,i} \in \mathbb{C}$ denotes the corresponding data symbol for the $i$th RF chain. The additive complex white Gaussian noise vector is defined as $\mathbf{n} \sim \mathscr{CN}(0, N_0\mathbf{I}_{N_r})$ with zero mean and $N_0$ variance. The received signal-to-noise ratio (SNR) at the $c$th subcarrier for the $i$th RF chain can be written as

$$\Gamma_{c,i} = \frac{\left|\mathbf{w}_n^H \mathbf{H}_{c,i}\mathbf{m}_n\right|^2}{\left\|\mathbf{w}_n\right\|^2 N_0}, \tag{12}$$

where $\mathbf{w}_n \in \mathbb{C}^{N_r}$ denotes the receive filter for the MRN, $\mathscr{M}$ is the set of steering vectors from which the optimal beamforming weight is selected.

## 4. Beamforming for Higher Operating Frequencies on Railway Networks

*4.1. Problem Formulation.* To maximize the received SNR on each RF chain, a joint transmit/receive beamforming is proposed; that is,

$$\begin{aligned} \underset{\{\mathbf{m}_n, \mathbf{w}_n\}}{\text{maximize}} \quad & \Gamma_{c,i} \\ \text{subject to} \quad & \mathbf{m}_n \in \mathscr{M} \\ & \mathbf{w}_n \in \mathscr{W}, \end{aligned} \tag{13}$$

where $\mathscr{M}$ and $\mathscr{W}$ are the sets of transmit and receive vectors.

If the channel is fully known at the BS and the MRN, the optimum weight is assumed to be solved by singular value decomposition (SVD). However, in a high mobility

scenario, full knowledge of the channel is not feasible. With no knowledge of the channel at the BS and MRN, a straightforward way to obtain the optimal weights is by an exhaustive search through the sets $\mathscr{M}$ and $\mathscr{W}$. But, in a real-time sensitive scenario like the HST, the selected weights will be outdated due to feedback delay. Due to property of the railway environment and the directionality of HFB propagation, the AoA and AoD of the LOS propagation path can be estimated based on the knowledge of the position of the train in a proactive manner. Hence we propose that the optimal beamforming weight $\mathbf{m}_n$ and receive filter $\mathbf{w}_n$ can be tied to the steering vectors such that

$$\begin{aligned}\mathbf{m}_n &= \mathbf{a}_t\left(\theta_{l_{\max}}^{\mathrm{AoD}}, \phi_{l_{\max}}^{\mathrm{AoD}}\right)\\ \mathbf{w}_n &= \mathbf{a}_r\left(\theta_{l_{\max}}^{\mathrm{AoA}}, \phi_{l_{\max}}^{\mathrm{AoD}}\right)\end{aligned} \tag{14}$$

and the sets $\mathscr{M}$ and $\mathscr{W}$ are composed of steering vectors from which the optimum vectors are selected. These sets are expressed as

$$\begin{aligned}\mathscr{M} &= \left\{\mathbf{a}_t\left(\theta_1, \phi_1\right), \ldots, \mathbf{a}_t\left(\theta_{N_b}, \phi_{N_b}\right)\right\}\\ \mathscr{W} &= \left\{\mathbf{a}_r\left(\theta_1, \phi_1\right), \ldots, \mathbf{a}_r\left(\theta_{N_b}, \phi_{N_b}\right)\right\}\\ &\qquad \theta_i, \phi_i \in [0, \pi),\ i = 1, 2, \ldots, N_b.\end{aligned} \tag{15}$$

We proposed that the beamform selection criteria will be tied to the velocity feedback as shown in Figure 2. The velocity feedback can be obtained using balises installed at roughly regular intervals along the track as shown in Figure 2. A balise is an electronic beacon or transponder placed between the rails of a railway as apart of an automatic train protection system. It is currently an integral part of the European train control system (ETCS) that gives the exact location of a train. They are also used in the Chinese train control system. Originally, the balises are safety equipment that transmit information about the location of the balise and the geometry of the track region to the next balise and speed restrictions.

The balise is capable of receiving information from the train, but currently this feature is rarely used. We propose that the fixed information (e.g., the geometry of the track) on each balise is made available at the BSs that cover the region of the track where these balises are placed, and once the HST crosses over a balise, the balise is activated and receives the HST speed information. The balise usually comes in pairs, which can be used to determine the direction of the HST (velocity) and this information along with the balise index number is fed back to the BS.

*4.2. High Speed Train Beamforming Selection Scheme.* The beam selection is based on anticipated AoD and AoA of the dominant path, which is calculated from the prior information of the rail environment. This information includes the horizontal distance between the BS and the track, the geometry of the track, the height of the BS, the height of the train and the speed of the train. Based on these, the angular domain can be determined by casting a normal three-dimensional positioning calculation to a single dimension

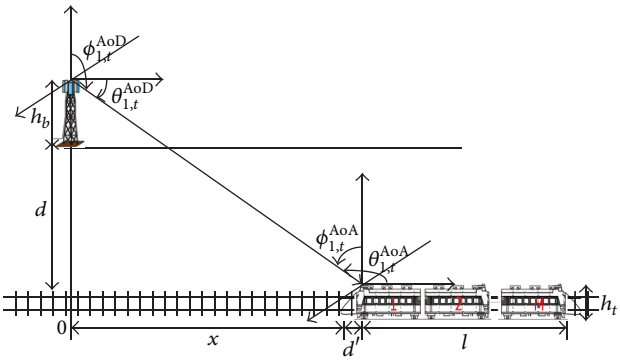


FIGURE 3: Determination of angle of arrival based on HST position.

and the sets of transmit and receive vectors $\mathscr{M}$ and $\mathscr{W}$ can be generated by evenly sampling the angular domain with a small interval.

Let us consider a section of the rail track as shown in Figure 3, with a horizontal distance $d$ between the BS and track. The height of the BS is $h_b$ meters above ground. The length of the train and height of the train plus antenna are denoted as $l$ and $h_t$, respectively.

Let $x$ be the initial horizontal coordinate distance between the front of the train and the BS. The BS is used as the origin of the spatial coordinates and reference point. The horizontal coordinate distance between the reference point and the $m$th receive antenna array of the $m$th MRN on top of the HST at position step $n$ is given as

$$x_{m,n} = \left(x + d'\right) - \left(\frac{m-1}{M}\right) l. \tag{16}$$

The formation of (16) depends on the shape of the train and the geometry of the rail track. The distance between the BS and the $m$th receive antenna array is defined as

$$d_{m,n} = \left\{x_{m,n}^2 + \left(h_b - h_t\right)^2 + d^2\right\}^{1/2}. \tag{17}$$

Based on the straight rail track, we assume the transmit antenna arrays at the BS are parallel to the the receive antenna arrays on the train; therefore the elevation angles are defined by the fixed height of the BS and train. Hence, the elevation angles of arrival and departure are assumed to be the same across the track and defined as

$$\begin{aligned}\phi_{m,n}^{\mathrm{AoA}} &= \sin^{-1}\left(\frac{\left\{d^2 + x_{m,1}^2\right\}^{1/2}}{d_{m,1}}\right)\\ &= \sin^{-1}\left(\frac{\left\{d^2 + x_{m,n}^2\right\}^{1/2}}{d_{m,n}}\right)\\ \phi_{m,n}^{\mathrm{AoD}} &= \pi - \phi_{m,1}^{\mathrm{AoA}} = \pi - \phi_{m,n}^{\mathrm{AoA}}.\end{aligned} \tag{18}$$

On the other hand, the azimuth angles are also a function of the horizontal coordinate distance $x_{m,t}$, which varies rapidly due to the speed of the train. The relationship between

**Input**:
BS retrieves initial HST position $x_{m,n}$
BS retrieves estimated velocity of the HST $v$
BS retrieves geometry of track and have $\mathscr{M}$
**Initialization**:
/*$M$: number of MRNs on the HST*/
(1) **for** $m \leq M$ **do**
(2) BS uses $\mathbf{m}_1^m$ based on initial location $x_{m,1}$
Train uses $\mathbf{w}_1^m$ based on initial location $x_{m,1}$
**Iteration**:
/*TTI: transmission time interval*/
(3) **for** ***each*** TTI **do**
(4) **for** $n < N_b$ **do**
(5) $\tau(n) = \|x_{1,n+1} - x_{1,1}\|/v$
(6) $i = 1$
/*$N_b$: number of beam direction in codebook*/
(7) **while** $i < N_b$ **do**
(8) CDT = $\tau(n+i)$
(9) Start CDT // count down in nanoseconds
(10) **if** CDT == 0 **then**
(11) **for** $m \leq M$ **do**
(12) BS uses next $\mathbf{m}_{n+i}^m$ based on initial location $x_{m,n+i}$
Train uses $\mathbf{w}_{n+i}^m$ based on initial location $x_{m,n+i}$
(13) $i = i + 1$
(14) Continue
(15) Update $v$

Algorithm 1: Proposed beamforming selection scheme (PBSS).

the azimuth angles and the horizontal coordinate distance can be expressed as

$$\theta_{m,n}^{\mathrm{AoA}} = \frac{\pi}{2} - \sin^{-1}\left(\frac{d}{d_{m,n}}\right)$$
$$\theta_{m,n}^{\mathrm{AoD}} = \pi - \theta_{m,n}^{\mathrm{AoA}}. \tag{19}$$

Therefore, with prior knowledge of $d_{m,n}$, the anticipated AoA and AoD of the dominant path can easily be computed for different sections of the rail track. Within a section of the track covered by the BS, the track is divided into $N_b$ position steps with the initial position of the train tagged at $n = 1$ and known at the BS. With knowledge of the velocity of the train, the BS estimates the time at which the train approaches the next position step $n$ and selects the appropriate beamforming weights and receive filters from the codebook generated using (18) and (19). The codebook sets $\mathscr{M}$ and $\mathscr{W}$ are ordered in a sequential way as in (10) such that, instead of an exhaustive search of the appropriate beams, a count-down-timer (CDT) is used to trigger the next beam to use in the codebook sets $\mathscr{M}$ and $\mathscr{W}$. The CDT is configured based on the known estimated velocity of the HST at the BS. The proposed scheme is summarized in Algorithm 1. The size of $N_b$ defines the level of quantized angles in $\mathscr{M}$ and $\mathscr{W}$.

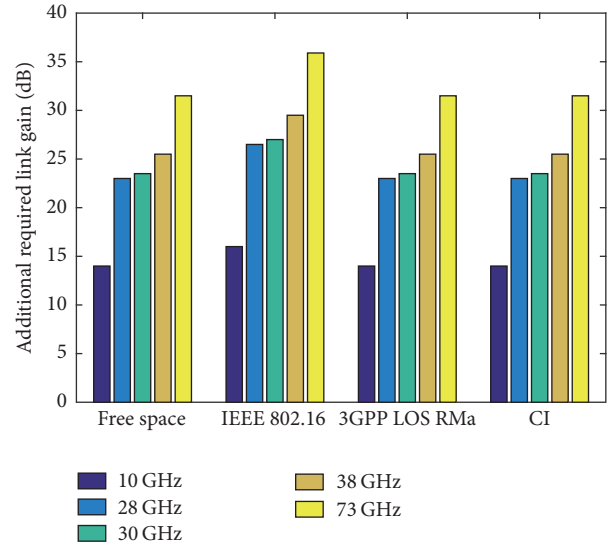


Figure 4: Additional required gain with respect to 2 GHz.

## 5. Performance Evaluation

*5.1. Required Pathloss Gains and SNR/SINR Lower Bound.* First, we briefly compare the effect on the pathloss observed for HFB signals with microwave frequency signals using conventional and higher frequency proposed pathloss models. To this end, we focus on the amount of gain required by HFB signals to maintain the same pathloss as for the microwave signals. Knowledge on the amount of gain required is particularly useful in the HST network, since it is important to be able to maintain the macrocell size currently used by microwave bands to avoid extreme frequent handover as the HST moves across multiple cells at high speed.

The required gain needed at carrier frequencies 10, 28, 30, 38, and 73 GHz to achieve the same pathloss with a carrier frequency of 2 GHz is shown in Figure 4 with a fixed link distance of 900 m.

The bar chart shows the additional gain required at HFBs to maintain the same pathloss as at 2 GHz operating frequency comparing the four different pathloss models examined in Section 2.3. For each of the pathloss models examined, it can be seen in Figure 4 that the higher the carrier frequency, the large the additional gain required to maintain same pathloss as the 2 GHz carrier frequency. It can also be observed that the required gains for the free space, IEE 802.16, and CI pathloss models are similar to the required gains approximately 14, 23, 24, 26, and 32 dB for carrier frequencies 10, 28, 30, 38, and 73 GHz, respectively. This shows that the pathloss models' dependencies on the carrier frequency are the same and since these three pathloss models exhibit a single slope curve, the dependencies on distance are also similar. The modified IEE 802.16 pathloss model has higher required gains compared to the other pathloss models as a result of a difference in the dependency of the carrier frequency.

Furthermore, the modified IEEE 802.16 pathloss model exhibits a varying dependency on distance with respect to

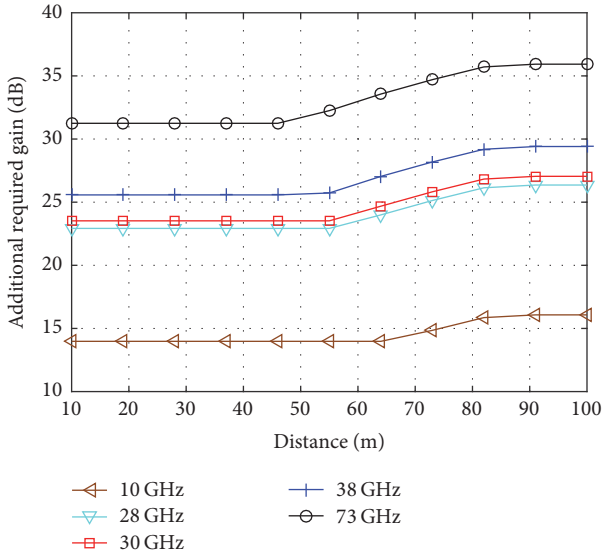


Figure 5: Modified IEEE 802.16: required gain with respect to 2 GHz.

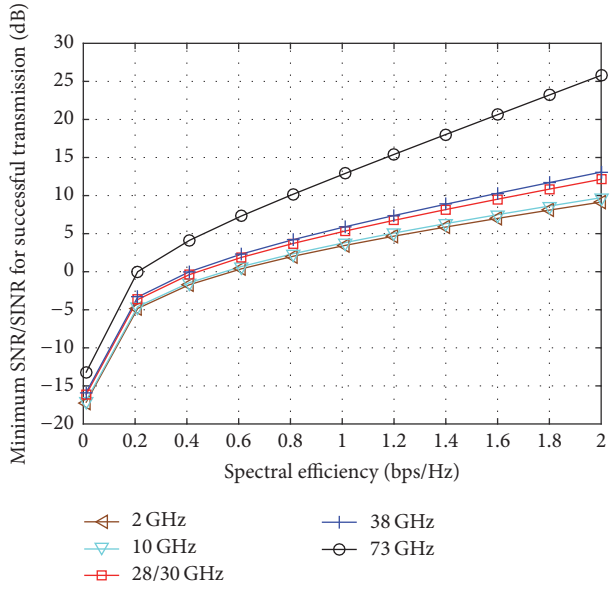


Figure 6: Lower bound on SINR for a given spectral efficiency.

Table 2: Obtaining the bandwidth efficiency factor for different frequency bands.

| Frequency (GHz) | 2 | 10 | 28 | 30 | 38 | 73 |
|---|---|---|---|---|---|---|
| $N_{cp}$ (%) | 7.15 | 8.94 | 28.27 | 28.27 | 33.7 | 65.44 |
| $N_{pilot}$ (%) | 4.76 | 5.56 | 4.35 | 4.35 | 4.17 | 4.37 |
| $N_{L1/L2}$ (%) | 28.5 | 28.5 | 28.5 | 28.5 | 28.5 | 28.5 |
| $N_{ACLR}$ (%) | 10 | 10 | 10 | 10 | 10 | 10 |
| $\alpha$ | 0.57 | 0.54 | 0.44 | 0.44 | 0.41 | 0.21 |

the carrier frequency as seen in Figure 5. The figure shows similar required gain for a range of distance, which changes with respect to the carrier frequency. As the carrier frequency increases, the range of distance which follows the free space pathloss pattern becomes shorter.

The required gains for HFBs to maintain the same pathloss as the 2 GHz frequency band are closely in the same range irrespective of the pathloss model used. If, for a given link distance, the required gain compensations for the HFBs are applied to achieve the same SNR across the frequency bands, the same target rate can be achieved at low mobility. However, due to the high mobility of the HST and the sensitivity to Doppler and delay spread by HFBs, large frame errors can occur. Hence a minimum SNR/SINR ratio for reliable communication at a given target rate needs to be defined taking into account the high mobility of the HST and the sensitivity to Doppler and delay spread by HFBs.

The minimum SNR/SINR required for successful demodulation of a transmitted signal is obtained using (1). The bandwidth efficiency factor given in Table 2 was derived from (2) and the 5G new radio parameters in Table 1.

The SNR efficiency factor was obtained from extrapolation from lookup table mapping between CQI and modulation scheme in [51]. Figure 6 shows the minimum required SNR/SINR ratios to achieve successful transmission with different spectral efficiencies.

The figure shows that, to achieve a 0.2 bps/Hz spectral efficiency, the observed SINR must be greater than −5 dB for the 2 GHz curve. For HFBs, the minimum SNR/SINR targets are higher, which show that the higher the carrier frequency the higher the sensitivity to high mobility. The figure also shows that, with the same SNR/SINR for the different frequencies, which can be achieved with the additional gain from Figure 4, the achievable spectral efficiency will vary with respect to frequency band. For example, with an SNR/SINR of 5 dB, the achievable spectral efficiency at 10 GHz is 1.2 bps/Hz and, at 73 GHz, the achievable spectral efficiency is 0.42 bps/Hz.

*5.2. SINR at Cell-Edge for Different Operating Frequencies.* We consider an interference limited scenario with the aim of evaluating the impact of intercell-interference (ICI) at different operating frequency bands. The achievable SINRs at the cell-edge are compared for the different frequency bands and pathloss models. A downlink transmission with only large scale fading is assumed using a 19 trisector cell hexagonal layout. The intersite-distance (ISD) was set to 1730 m with a frequency reuse pattern of 1-3-1, where all the adjacent cells use the same frequency set in order to ensure ICI. We also assumed a load factor of 1, which is the ratio between the used bandwidth and the available bandwidth for the interfering links.

The results in Figure 7 show that the achievable SINR at the cell-edge decreases as the bandwidth increases, since the noise power is a function of the bandwidth. In general, the results show a small reduced difference in the achievable SINR for HFBs compared to the 2 GHz carrier frequency except for the modified IEEE 802.16 pathloss model. The effects of higher operating frequencies on the SINR are significant when considering the IEEE 802.16 pathloss model,

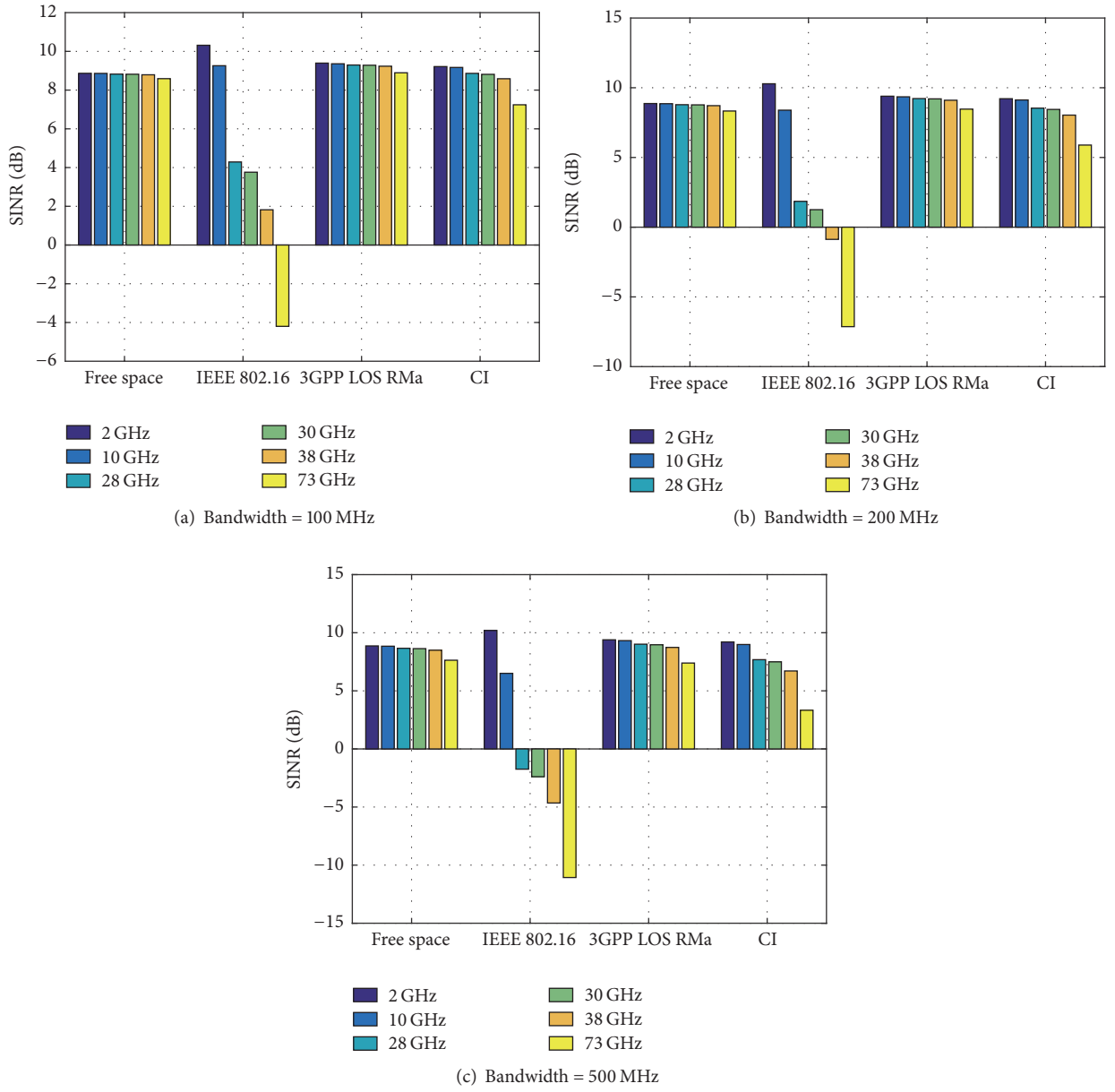


Figure 7: Achievable SINR at cell-edge for different operating frequencies at different bandwidth.

which is as a result of the varying increase in pathloss with respect to distance and frequency as reflected in Figure 5. Considering the three other pathloss models, there is a minimum of 14 dB additional pathloss compared to the 2 GHz frequency band. However, in an interference limited scenario as observed in Figure 7(c), the maximum reduction in achievable SINR at the cell-edge compared to the 2 GHz frequency band shows about 6 dB loss for a bandwidth of 500 MHz. This is as a result of the fact that, at higher operating frequencies, the interfering paths also experience increased pathloss. Hence, in an interference limited network, the reduced interference in the network layout reduces the effect of the increased pathloss on the desired path. Note that the spectral efficiency for a given SINR will vary according to Figure 6.

*5.3. Proposed Beam Forming Scheme Evaluation.* The beamform simulation model consists of a single BS with $N_{\text{rf}}$ RF chains and $N_t$ transmit antennas serving the HST. Each carriage is equipped with an MRN having $N_r$ receive antennas. The number of subcarriers is set to $C = 7500$ with a subcarrier spacing of 60 kHz for 28 GHz carrier frequency. Based on (14), we only consider RMa propagation with LOS type of condition. The channel coefficients are generated based on a statistical spatial channel model (SSCM) for HFB LOS communication links [50]. It is based on extensive

Table 3: Simulation parameters.

| Parameters | Values |
|---|---|
| Carrier frequency | 28 GHz |
| Number of channel realizations | 100 |
| BS antenna spacing | 0.5 wavelength |
| Length of each carriage | 30 m |
| Number of BS/MRN antennas | 4, 8, 16, 32 |
| Angle of arrival/departure | Uniform distribution $(-\pi/2, \pi/2)$ |
| Transmit power $P_t$ | 46 dBm |

propagation measurements carried out on 28 and 73 GHz band. In each simulation, the performance is averaged over 100 independent channel realizations. The main simulation parameters are listed in Table 3.

Based on this set-up, we evaluate the performance of the proposed beamform selection scheme (PBSS) and compare with the ideal SVD technique and the state-of-the-art LTE closed-loop transmission technique for the case where $N_t = 4$. We also consider the impact of multistream transmission with the proposed beamform approach with the assumption that the number of multistream transmissions is equal to the number of RF chains. For the PBSS, we consider the case where the beam gain is only at the transmitter side and proportional to the number of antennas. Unity gain is assumed at the receiver side in order to minimize beam misalignment between the BS and HST since the beam gain is inversely proportional to the beamwidth. For the performance comparison, we assumed there was no error in the estimated AoA and AoD.

Figure 8 shows the data rates achieved for different SNR values with the SVD beamforming scheme and the proposed beamforming selection scheme (PBSS) under LOS channel condition, where $N_t = N_r = 4$ and $N_{\text{rf}} = 1$ for single-stream and $N_{\text{rf}} = 4$ for multistream PBSS transmission. The data rate of the LTE closed-loop scheme is also shown in the figure.

The multistream SVD scheme provides the optimum performance, since perfect knowledge of the channel is assumed to be known and power can be allocated via water-filling to the possible number of streams, which is limited by $\min(N_t, N_r)$. However, the performance of the single-stream SVD is at par with the multistream SVD as a result of the limited multipath components (MPCs) exhibited by the HFB channel. With the accurate estimate of the AoA/AoD of the strongest MPC, the single-stream PBSS is able to achieve a close performance to the SVD scheme. The multistream PBSS scheme considers a fixed number of RF chains ($N_{\text{rf}} = 4$) with equal power allocation across the RF chains. Due to knowledge of only the AoA/AoD and the small number of limited MPCs, the rate performance of the multistream PBSS scheme deteriorate significantly as observed in Figure 8. The state-of-the-art LTE closed-loop scheme in which the best possible transmission rank and precoder are selected for transmission with equal power allocation shows a rate performance not as good as the PBSS rate performance as seen in Figure 8.

Figure 9 shows the data rates achieved for different SNR values with the SVD beamforming scheme and the

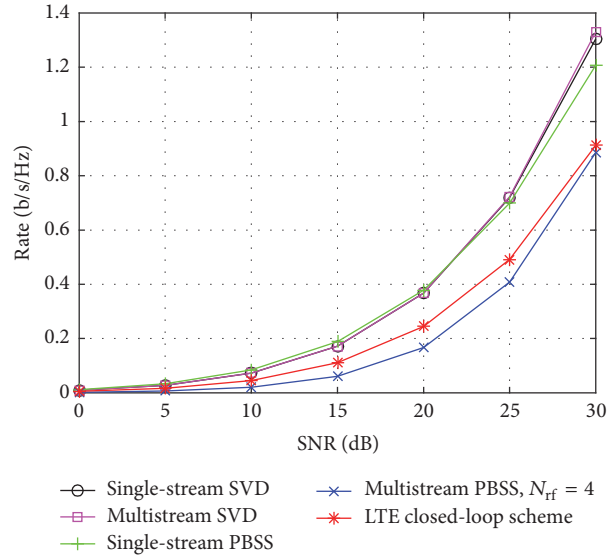


Figure 8: Rate performance for different beamforming techniques with $N_t = 4$ and $N_r = 4$.

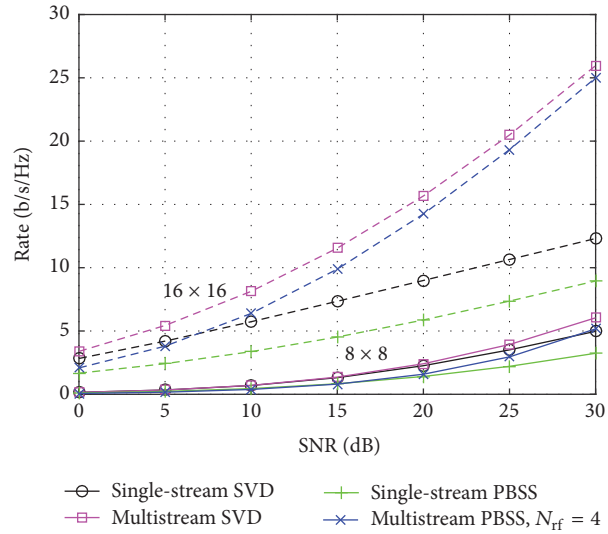


Figure 9: Rate performance for different beamforming techniques with $N_t = 8/16$ and $N_r = 8/16$.

proposed beamforming selection scheme (PBSS), both for single-stream and for multistream transmission with $8 \times 8$ and $16 \times 16$ HFB LOS SSCM channel. The results show a significant increase in spectral efficiency as the antenna array increases from 8 to 16 at both BS and HST. At low SNR, the performances of all the schemes are roughly similar. However, as the SNR increases the performance gap becomes evident. For example, considering the $8 \times 8$ and $16 \times 16$ channel at a SNR of 5 dB, the maximum differences in achieved rate across the schemes are 0.06 b/s/Hz and 3 b/s/Hz, respectively. Correspondingly, at a SNR of 25 dB, the maximum differences in achieved rates are 2 b/s/Hz and 13 b/s/Hz. This result implies that performance improvement from spatial diversity becomes significant with large antenna

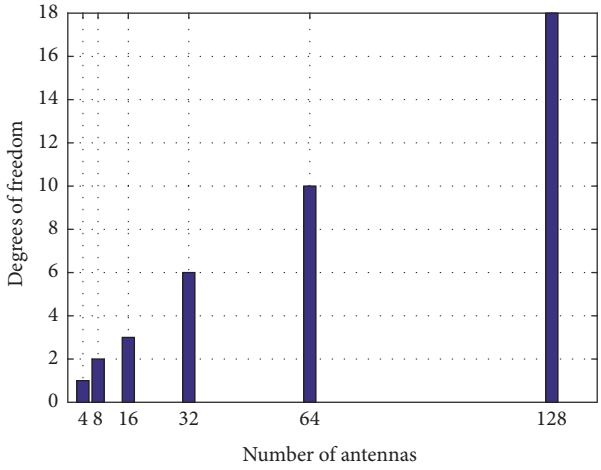


Figure 10: Average spatial degrees of freedom extracted from SSCM channel with different number of antennas.

arrays and high SNR. The significant increase in performance of the multistream SVD compared to the single-stream SVD for higher number of transmit and receive antennas is as a result of the additional spatial degrees of freedom being exploited by the multistream SVD scheme. From this figure, it is also observed that, with an increase in the number of transmit and receive antennas, the rate performance of the single-stream PBSS drops significantly for high SNR value compared to the multistream SVD performance. However, the rate performance of the multistream PBSS shows a close performance to the multistream SVD for the $16 \times 16$ channel.

Figure 10 shows the average number of spatial degrees of freedom observed from different number of transmit antennas used in generating 100 SSCM channel realizations. From the figure, it can be seen that as the number of antennas increases, the spatial degrees of freedom or resolvable MPC increase unlike the assumptions made in [18], where the number of resolvable MPCs is fixed and significantly small irrespective of the number of antennas used. However, Figure 10 shows that the number of MPCs is significantly small in relation to the size of the antenna array at the BS and on the HST, but it grows with increase in the size of the antenna array. The use of large antenna array on the roof top of the HST can easily be implemented due to the large length of the train carriages.

Note that the SSCM channel model used here is based on field measurements using the TCSL framework to model the channel through separate time clusters that have time-delay statistics and through spatial lobes which represent the strongest directions of multipath arrival [50]. Each time cluster consists of MPCs travelling close in time but arriving from different directions. Hence the number of resolvable MPCs which is modelled randomly is also a function of the number of antennas.

It can be observed from Figure 8 that the single-stream PBSS shows a performance equivalent to the multistream PBSS due to the small spatial degrees of freedom exhibited by the channel as reflected in Figure 10. As the antenna array grows large, the beamforming gains exploited by the single-stream PBSS are limited by the increasing potential in the spatial diversity as observed in Figure 9. With large antenna array, the multistream PBSS addresses the shortcoming of the single-stream PBSS, which can be explained in terms of trade-off between beamforming gains and spatial gains. That is, the large antenna array is divided into subarrays such that each subarray shares a single RF chain. Hence, each subarray has a fraction of the beamforming gain but multiple times the spatial gains. Therefore, increasing the number of RF chains in proportion to the number of antennas used can significantly improve the rate performance without additional complexity. The performance gap between the multistream SVD and the multistream PBSS in Figure 9 shows an achieved spectral efficiency difference of around 0.5 b/s/Hz and 1.6 b/s/Hz for $8 \times 8$ and $16 \times 16$ channels. This results from the fact that, with larger number of antennas, the channel is defined by a larger number of MPCs arriving from different directions and the multistream PBSS uses only the predicted LOS component AoA/AoD to define the beamforming weights.

## 6. Conclusion

In the development of 5G networks for HST communications, HFBs will play an important role in providing high data rates to train passengers. Hence, in this paper we examined the feasibility of using HFBs with respect to the 2 GHz band for HST networks. We modified the OFDM frame structure such that the characteristics of HFBs and high velocity of the HST are taken into consideration. With the modified frame structure, we established a lower bound on the SNR/SINR for a given target spectral efficiency needed to achieve successful and reliable communication. The lower bound on the SNR/SINR varies with the different frequency bands examined. Based on the OFDM frame structure, the symbol length is shortened with an increase in the carrier frequency, thereby increasing the sensitivity to both ISI and ICI. A fixed cyclic prefix length was used to compensate for the effect of both ISI and ICI, but at the cost of a significant amount of bandwidth consumed, particularly evident at the 73 GHz frequency band. We also showed that, irrespective of the pathloss model used, the pathloss dependencies on frequency and distance are similar when evaluated in terms of the required gain by HFBs to achieve the same performance at microwave band. This is motivated by the fact that there are many existing and ongoing campaign efforts towards 5G pathloss modelling [52] and it will be important to understand the impact of the choice of pathloss model used. Then, we formulated and developed a sequentially ordered codebook based on the array response vector/analogue beamforming and proposed a time-based analogue beamforming selection algorithm for HST without the need for training overhead. The performance of the proposed algorithm was evaluated and results show an achievable spectral efficiency comparable to the ideal SVD scheme with a reduced performance gap of less than 2 b/s/Hz.

The results provided in this paper demonstrate the potential of the use of HFBs for HST networks. However,

a maximum carrier frequency of 38 GHz is suggested for HST due to the increased sensitivity to Doppler shift, ISI, and ICI at HFBs. For future work, we will consider the application of variable cyclic prefix length to improve the spectral efficiency. We will also consider the impact of velocity estimation error and AoA/AoD estimation error on the proposed beamforming selection scheme.

## Conflicts of Interest

The authors declare that they have no conflicts of interest.

## Acknowledgments

This work was supported by the Finnish Funding Agency for Technology and Innovation, Nokia, Keysight Technologies, and Huawei Technologies.

## References

[1] Cisco, "Cisco visual networking index: forecast and methodology, 2016 to 2021," White Paper, 2017, https://www.cisco.com/c/en/us/solutions/collateral/service-provider/visual-networking-index-vni/complete-white-paper-c11-481360.pdf.

[2] X. Zhu, S. Chen, H. Hu, X. Su, and Y. Shi, "TDD-based mobile communication solutions for high-speed railway scenarios," *IEEE Wireless Communications*, vol. 20, no. 6, pp. 22–29, 2013.

[3] É. Masson, M. Berbineau, and S. Lefebvre, "Broadband internet access on board high speed trains, a technological survey," *International Workshop on Communications Technologies for Vehicles*, Article ID Springer, pp. 165–176, 2015.

[4] F. Boccardi, B. Clerckx, A. Ghosh et al., "Multiple-antenna techniques in LTE-advanced," *IEEE Communications Magazine*, vol. 50, no. 3, pp. 114–121, 2012.

[5] W. Roh, J.-Y. Seol, J. Park et al., "Millimeter-wave beamforming as an enabling technology for 5G cellular communications: theoretical feasibility and prototype results," *IEEE Communications Magazine*, vol. 52, no. 2, pp. 106–113, 2014.

[6] J. Wang, Z. Lan, C.-W. Pyo et al., "Beam codebook based beamforming protocol for multi-Gbps millimeter-wave WPAN systems," *IEEE Journal on Selected Areas in Communications*, vol. 27, no. 8, pp. 1390–1399, 2009.

[7] T. S. Rappaport, Y. Qiao, J. I. Tamir, J. N. Murdock, and E. Ben-Dor, "Cellular broadband millimeter wave propagation and angle of arrival for adaptive beam steering systems (invited paper)," in *Proceedings of IEEE Radio and Wireless Symposium (RWS), 2012*, pp. 151–154, 2012.

[8] P. T. Dat, A. Kanno, N. Yamamoto, and T. Kawanishi, "WDM RoF-MMW and linearly located distributed antenna system for future high-speed railway communications," *IEEE Communications Magazine*, vol. 53, no. 10, pp. 86–94, 2015.

[9] A. Maltsev, A. Sadri, A. Pudeyev, and I. Bolotin, "Highly directional steerable antennas: high-gain antennas supporting user mobility or beam switching for reconfigurable backhauling," *IEEE Vehicular Technology Magazine*, vol. 11, no. 1, pp. 32–39, 2016.

[10] J. N. Murdock, E. Ben-Dor, Y. Qiao, J. I. Tamir, and T. S. Rappaport, "A 38 GHz cellular outage study for an urban outdoor campus environment," in *Proceedings of the IEEE Wireless Communications and Networking Conference (WCNC '12)*, pp. 3085–3090, Shanghai, China, 2012.

[11] Y. Azar, G. N. Wong, K. Wang et al., "28 GHz propagation measurements for outdoor cellular communications using steerable beam antennas in New York city," in *Proceedings of the IEEE International Conference on Communications (ICC '13)*, pp. 5143–5147, Budapest, Hungary, June 2013.

[12] T. S. Rappaport, F. Gutierrez, E. Ben-Dor, J. N. Murdock, Y. Qiao, and J. I. Tamir, "Broadband millimeter-wave propagation measurements and models using adaptive-beam antennas for outdoor Urban cellular communications," *IEEE Transactions on Antennas and Propagation*, vol. 61, no. 4, pp. 1850–1859, 2013.

[13] A. Alkhateeb, O. El Ayach, G. Leus, and R. W. Heath, "Channel estimation and hybrid precoding for millimeter wave cellular systems," *IEEE Journal on Selected Topics in Signal Processing*, vol. 8, no. 5, pp. 831–846, 2014.

[14] S. Sun, T. S. Rappaport, R. W. Heath, A. Nix, and S. Rangan, "MIMO for millimeter-wave wireless communications: beamforming, spatial multiplexing, or both?" *IEEE Communications Magazine*, vol. 52, no. 12, pp. 110–121, 2014.

[15] S. Hur, T. Kim, D. J. Love, J. V. Krogmeier, T. A. Thomas, and A. Ghosh, "Millimeter wave beamforming for wireless backhaul and access in small cell networks," *IEEE Transactions on Communications*, vol. 61, no. 10, pp. 4391–4403, 2013.

[16] T. Kim, J. Park, J.-Y. Seol, S. Jeong, J. Cho, and W. Roh, "Tens of Gbps support with mmWave beamforming systems for next generation communications," in *Proceedings of the 2013 IEEE Global Communications Conference, GLOBECOM 2013*, pp. 3685–3690, 2013.

[17] O. E. Ayach, R. W. Heath Jr., S. Abu-Surra, S. Rajagopal, and Z. Pi, "The capacity optimality of beam steering in large millimeter wave MIMO systems," in *Proceedings of the 2012 IEEE 13th International Workshop on Signal Processing Advances in Wireless Communications, SPAWC 2012*, pp. 100–104, 2012.

[18] Z. Xiao, T. He, P. Xia, and X.-G. Xia, "Hierarchical codebook design for beamforming training in millimeter-wave communication," *IEEE Transactions on Wireless Communications*, vol. 15, no. 5, pp. 3380–3392, 2016.

[19] H. Song, X. Fang, and Y. Fang, "Millimeter-Wave network architectures for future high-speed railway communications: challenges and solutions," *IEEE Wireless Communications*, vol. 23, no. 6, pp. 114–122, 2016.

[20] B. Ai, K. Guan, M. Rupp et al., "Future railway services-oriented mobile communications network," *IEEE Communications Magazine*, vol. 53, no. 10, pp. 78–85, 2015.

[21] Y. Cui, X. Fang, and L. Yan, "Hybrid spatial modulation beamforming for mmWave railway communication systems," *IEEE Transactions on Vehicular Technology*, vol. 65, no. 12, pp. 9597–9606, 2016.

[22] J. Kim and A. F. Molisch, "Enabling Gigabit services for IEEE 802.11ad-capable high-speed train networks," in *Proceedings of IEEE Radio and Wireless Symposium (RWS)*, pp. 145–147, 2013.

[23] V. Va, X. Zhang, and R. W. Heath, "Beam switching for millimeter wave communication to support high speed trains," in *Proceedings of the 82nd IEEE Vehicular Technology Conference (VTC Fall)*, pp. 1–5, 2015.

[24] G. R. MacCartney, S. Sun, T. S. Rappaport et al., "Millimeter wave wireless communications," in *Proceedings of the the 5th Workshop*, pp. 31–36, New York, NY, USA, 2016.

[25] 3GPP, "3rd generation partnership project; technical specification group radio access network; study on channel model for frequency spectrum above 6 GHz," Rep. TR 38.900 v14.1.0, 2016.

[26] S. Sun, T. S. Rappaport, T. A. Thomas et al., "Investigation of Prediction Accuracy, Sensitivity, and Parameter Stability of

Large-Scale Propagation Path Loss Models for 5G Wireless Communications," *IEEE Transactions on Vehicular Technology*, vol. 65, no. 5, pp. 2843–2860, 2016.

[27] R. He, B. Ai, G. Wang et al., "High-Speed railway communications: from GSM-R to LTE-R," *IEEE Vehicular Technology Magazine*, vol. 11, no. 3, pp. 49–58, 2016.

[28] T. Zhou, C. Tao, S. Salous, L. Liu, and Z. Tan, "Channel sounding for high-speed railway communication systems," *IEEE Communications Magazine*, vol. 53, no. 10, pp. 70–77, 2015.

[29] R. He, Z. Zhong, and B. Ai, "Path loss measurements and analysis for high-speed railway viaduct scene," in *Proceedings of the 6th International Wireless Communications and Mobile Computing Conference, IWCMC 2010*, pp. 266–270, 2010.

[30] R. He, Z. Zhong, B. Ai, G. Wang, J. Ding, and A. F. Molisch, "Measurements and analysis of propagation channels in high-speed railway viaducts," *IEEE Transactions on Wireless Communications*, vol. 12, no. 2, pp. 794–805, 2013.

[31] R. He, Z. Zhong, B. Ai, and J. Ding, "Measurements and analysis of short-term fading behavior for high-speed rail viaduct scenario," in *Proceedings of the 2012 IEEE International Conference on Communications, ICC 2012*, pp. 4563–4567.

[32] R. He, Z. Zhong, B. Ai, J. Ding, Y. Yang, and A. F. Molisch, "Short-term fading behavior in high-speed railway cutting scenario: Measurements, analysis, and statistical models," *IEEE Transactions on Antennas and Propagation*, vol. 61, no. 4, pp. 2209–2222, 2013.

[33] F. Luan, Y. Zhang, L. Xiao, C. Zhou, and S. Zhou, "Fading characteristics of wireless channel on high-speed railway in hilly terrain scenario," *International Journal of Antennas and Propagation*, vol. 2013, Article ID 378407, 9 pages, 2013.

[34] P. Aikio, R. Gruber, and P. Vainikainen, "Wideband radio channel measurements for train tunnels," in *Proceedings of IEEE Vehiclar Technology Conference*, pp. 460–464, 1998.

[35] J. Meinilä, P. Kyösti, T. Jämsä, and L. Hentilä, "WINNER II Channel Models," *Information Society Technologies*, 2008.

[36] 3GPP, "3rd generation partnership project; technical specification group radio access network; study on scenarios and requirements for next generation access technologies," Rep. TR 38.913 v14.2.0, 2016.

[37] A. O. Laiyemo, H. Pennanen, P. Pirinen, and M. Latva-aho, "Transmission strategies for throughput maximization in high-speed-train communications: from theoretical study to practical algorithms," *IEEE Transactions on Vehicular Technology*, vol. 66, no. 4, pp. 2997–3011, 2017.

[38] M. K. Müller, M. Taranetz, and M. Rupp, "Providing current and future cellular services to high speed trains," *IEEE Communications Magazine*, vol. 53, no. 10, pp. 96–101, 2015.

[39] RYSAVY Research, "Mobile broadband transformation: LTE to 5G" White Paper, 2016, http://www.5gamericas.org/files/2214/7257/3276/Final_Mobile_Broadband_Transformation_Rsavy_whitepaper.pdf.

[40] P. Mogensen, W. Na, I. Z. Kováes et al., "LTE capacity compared to the Shannon bound," in *Proceedings of IEEE 65th Vehicular Technology Conference (VTC)*, pp. 1234–1238, 2007.

[41] S. Sesia, M. Baker, and I. Toufik, *LTE-the UMTS Long Term Evolution: from Theory to Practice*, 2011.

[42] J. Zyren and W. McCoy, "Overview of the 3GPP long term evolution physical layer," *Freescale Semiconductor, Inc., White Paper*, 2007.

[43] A. Goldsmith, Wireless Communications, Cambridge University, in press, 2005.

[44] M. Naden and M. Hart, "Multihop path loss model (base-to-relay and base-to-mobile)," *IEEE*, vol. 43, 2006.

[45] G. Senarath, "Multi-hop relay system evaluation methodology (channel model and performance metric)," 2007, http://ieee802.org/16/relay/docs/80216j-06_013r3.pdf.

[46] M. Gudmundson, "Correlation model for shadow fading in mobile radio systems," *Electronics Letters*, vol. 27, no. 23, pp. 2145-2146, 1991.

[47] H. Omote and T. Fujii, "Empirical arrival angular profile prediction formula for mobile communication systems," in *Proceedings of IEEE 65th Vehicular Technology Conference (VTC)*, pp. 599–603, 2007.

[48] W. Dong, J. Zhang, X. Gao, P. Zhang, and Y. Wu, "Cluster identification and properties of outdoor wideband mimo channel," in *Proceedings of IEEE 66th Vehicular Technology Conference (VTC)*, pp. 829–833, 2007.

[49] T. S. Rappaport, G. R. MacCartney, M. K. Samimi, and S. Sun, "Wideband millimeter-wave propagation measurements and channel models for future wireless communication system design," *IEEE Transactions on Communications*, vol. 63, no. 9, pp. 3029–3056, 2015.

[50] M. K. Samimi and T. S. Rappaport, "3-D millimeter-wave statistical channel model for 5g wireless system design," *IEEE Transactions on Microwave Theory and Techniques*, vol. 64, no. 7, pp. 2207–2225, 2016.

[51] 3GPP, "3rd generation partnership project; technical specification group radio access network; evolved universal terrestrial radio access (E-UTRA); physical layer procedures," Rep. TS 36.213 v14.1.0, 2016.

[52] K. Haneda, L. Tian, H. Asplund et al., "Indoor 5G 3GPP-like channel models for office and shopping mall environments," in *Proceedings of IEEE International Conference on Communications Workshops (ICC)*, pp. 694–699, 2016.